




Article

Revealing the Dynamic Transformation of Austenite to Bainite during Uniaxial Warm Compression through In-Situ Synchrotron X-ray Diffraction

William Lemos Bevilaqua^{1,2,*}, J  r  my Epp^{3,4} , Heiner Meyer³ , Juan Dong³, Hans Roelofs⁵, Alexandre da Silva Rocha¹ and Afonso Reguly¹ 

- ¹ Post-Graduation Program in Mining, Metallurgical and Materials Engineering (PPGE3M), Federal University of Rio Grande do Sul (UFRGS), Av. Bento Gonalves, 9500, Porto Alegre 91501-970, Brazil; alexandre.rocha@ufrgs.br (A.d.S.R.); areguly@gmail.com (A.R.)
- ² Industrial Technical College, Federal University of Santa Maria (UFSM), Av. Roraima, 1000, Santa Maria 97105-900, Brazil
- ³ Leibniz Institute for Materials Engineering-IWT Bremen, Badgasteiner Str. 3, 28359 Bremen, Germany; epp@iwt-bremen.de (J.E.); hmeyer@iwt-bremen.de (H.M.); dong@iwt-bremen.de (J.D.)
- ⁴ MAPEX Center for Materials and Processes, University of Bremen, Badgasteiner Str. 3, 28359 Bremen, Germany
- ⁵ R&D, Swiss Steel AG, Emmenweidstr. 90, 6020 Emmenbr ucke, Switzerland; hroelofs@swiss-steel.com
- * Correspondence: william.bevilaqua@ufrgs.br



Citation: Bevilaqua, W.L.; Epp, J.; Meyer, H.; Dong, J.; Roelofs, H.; da Silva Rocha, A.; Reguly, A. Revealing the Dynamic Transformation of Austenite to Bainite during Uniaxial Warm Compression through In-Situ Synchrotron X-ray Diffraction. *Metals* **2021**, *11*, 467. <https://doi.org/10.3390/met11030467>

Academic Editor: Soran Biroscu

Received: 3 February 2021

Accepted: 5 March 2021

Published: 12 March 2021

Publisher's Note: MDPI stays neutral with regard to jurisdictional claims in published maps and institutional affiliations.



Copyright:   2021 by the authors. Licensee MDPI, Basel, Switzerland. This article is an open access article distributed under the terms and conditions of the Creative Commons Attribution (CC BY) license (<https://creativecommons.org/licenses/by/4.0/>).

Abstract: In this work, the microstructural evolution during the dynamic transformation of austenite to bainite was directly observed by in-situ high energy synchrotron X-ray diffraction measurements during warm uniaxial compression performed at the P07 beamline of PETRA III, DESY (Deutsches Elektronen-Synchrotron). Plastic deformation triggers the phase transformation, which is continuously stimulated by the introduction of dynamic dislocations into the austenite. This scenario accelerates the kinetics of bainite formation in comparison with conventional isothermal treatment. No mechanical stabilization of austenite was observed during dynamic transformation. Evidence of carbon partitioning between phases during plastic deformation was obtained. Further post-process investigations suggest that the bainitic microstructure developed during compression is oriented perpendicular to the loading direction. The findings open up new possibilities to design carbide-free bainitic microstructures directly via thermomechanical processing.

Keywords: dynamic transformation; thermomechanical processing; bainite; in-situ X-ray diffraction

1. Introduction

Although the thermomechanical processing of advanced bainitic steels has received considerable attention recently [1–8], knowledge on the dynamic transformation of austenite to bainite (in the present work referred as “ $DT_{(\gamma \rightarrow \alpha b)}$ ”) is limited. This non-conventional path for bainitic transformation was only evidenced by deviations in the stress-strain curves during ausforming experiments usually below 500  C [3,4,8,9]. So far, the $DT_{(\gamma \rightarrow \alpha b)}$ understanding is unclear in terms of kinetics, changes in lattice parameter, partitioning behavior of alloying elements, and the attainable volume fraction of bainitic ferrite during the deformation cycle. Such lack of experimental data restricts the possibility of exploiting $DT_{(\gamma \rightarrow \alpha b)}$ in new thermomechanical routes concepts, as well as microstructural modeling.

The study of $DT_{(\gamma \rightarrow \alpha b)}$ by conventional methods like dilatometry makes a precise determination of the phase content evolution during deformation difficult due to the superimposed effects of transformation-induced length increase and the reduction of sample length. To date, although several in-situ diffraction experiments have been conducted to investigate the mechanisms of the bainitic transformation in steels (under isothermal [10–14] or continuous cooling treatments [1,15–17]), real-time data of the microstructural evolution during ongoing $DT_{(\gamma \rightarrow \alpha b)}$ were not reported elsewhere.

Since in-situ high energy X-Ray diffraction (HEXRD) experiments allow for obtaining time-resolved precise quantitative information about complex phase transformations [18,19], it is thus the only technique in which the microstructural evolution of the $DT_{(\gamma \rightarrow \alpha b)}$ can be accurately studied during plastic deformation. Therefore, in the present investigation, HEXRD experiments were employed to build a detailed understanding of the microstructural evolution during $DT_{(\gamma \rightarrow \alpha b)}$ in a carbide-free bainitic steel.

2. Materials and Methods

The thermomechanical processing route shown in Figure 1a was applied in a carbide-free bainitic steel (0.16C–1.48Mn–1.22Si–1.19Cr–0.27Mo–0.12Cu–0.01V (Mass.%)), in which the estimated bainite start temperature is 528 °C according to the empirical expression proposed by Bohemen [20]. The treatments were performed using a modified dilatometer (DIL805A/D—TA-Instruments Inc., New Castle, DE, USA) coupled to angle-dispersive synchrotron X-ray diffraction measurements in transmission geometry with an energy of 98.188 keV at beamline P07-EH3 of Petra III, DESY/HZG, Germany—Hamburg.

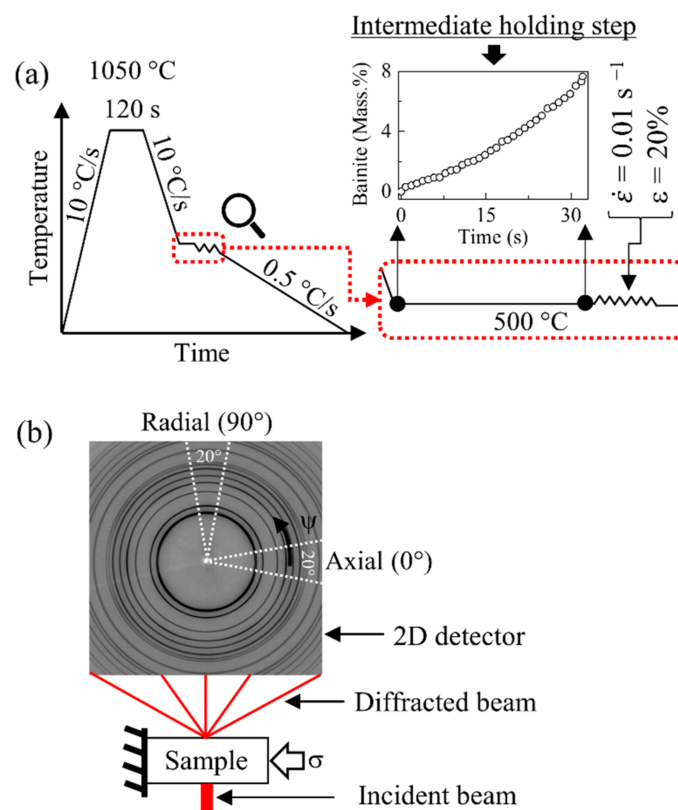


Figure 1. (a) Scheme of the thermomechanical cycle. The inset of (a) shows the intermediate holding step at 500 °C (with the resulting volume fraction of bainite determined from the synchrotron diffraction patterns), and deformation parameters; (b) experimental setup for the in-situ X-ray diffraction experiments.

Cylindrical samples (5 mm diameter and 10 mm length) were heated up to 1050 °C, held for 120 s and then cooled down to 500 °C. An intermediate holding step was applied to produce a small volume fraction of bainitic ferrite (≈ 8 Mass.% in a total time of 32 s—see the inset of Figure 1a) before the deformation step. Subsequently, the decomposition kinetics of austenite to bainite was tracked as a function of strain during uniaxial compression. This thermomechanical schedule allows studying precisely the evolution of DT kinetics from elastic to plastic deformation. After deformation, the specimen was held at 500 °C for five seconds (without any load) and then cooled to room temperature. For comparison, an

isothermal treatment at 500 °C (without deformation) was performed following the same time–temperature schedule presented in Figure 1a.

The deformation parameters (temperature, strain (ϵ) and strain rate ($\dot{\epsilon}$)) were selected considering technical limitations of the dilatometer. A thin molybdenum foil was placed in between the holders and the sample to reduce the friction and the thermal gradient. The heating and controlled cooling procedures were conducted using an induction coil and blowing argon into the sample, respectively. The temperature was measured with a type S thermocouple welded to the central part of the specimen next to the position of the incident X-ray beam. The configuration of the in situ experiments is shown in Figure 1b. Full diffraction rings were collected (throughout the thermomechanical treatment) in transmission geometry by a XRD 1621 area detector (PerkinElmer Inc., Waltham, MA, USA) with a measuring frequency of 5 Hz. The distance from the sample to the detector was nominally 1384 mm, and the size of the incident X-ray beam was 1 mm \times 1 mm. The detector calibration and the instrumental effects were obtained with a LaB₆ standard powder sample with 6 mm thickness, which corresponds to the final sample thickness after deformation.

The collected 2D data were converted to conventional 1D diffraction patterns in the software *pyFAI* version 0.19.0 of ESRF [21]. Full azimuthal integration of the diffraction rings was carried out to get the best possible statistics to calculate the phase fractions, while the average lattice parameter of each phase was determined considering cake portions of 20° in two azimuthal directions according to the schematic representation in Figure 1b. The phase fraction and the lattice parameters were quantified by the convolution-based Rietveld refinement implemented in TOPAS version 4.2 (Bruker AXS, Karlsruhe, Germany), taking into account the first ten $\{hkl\}$ reflections in the 2θ range from 2° to 8.4°.

A single peak fit procedure (applying a Pseudo-Voigt function) was implemented for the extraction of the 2θ positions and the full width at half maximum (FWHM) of the $\{220\}\gamma$ and $\{211\}\alpha$ reflections. The reason for this choice is to avoid any possible overlap with other peaks in the diffraction pattern. Besides, these reflections are often chosen to provide additional information about the microstructure evolution (e.g., [1,15,22,23]). The lattice strains ($\epsilon_{i\{hkl\}}$) in each phase were calculated during the deformation step using the same angular range as described earlier for the lattice parameters, according to:

$$\epsilon_{i\{hkl\}} = \frac{d_{i\{hkl\}} - d_{0\{hkl\}}}{d_{0\{hkl\}}} \quad (1)$$

where d_i is the measured d -spacing during the strain evolution, and d_0 is the reference lattice spacing before deformation.

After the in situ experiments, the specimens were sectioned in the longitudinal cross-section and prepared by standard metallographic procedures (grinding, polishing, and etching using Nital 3% solution). The microstructure was examined under a VEGA II XLH scanning field-emission electron microscope–SEM (TESCAN, Brno, Czech Republic) in the region corresponding to the incident area of the X-ray beam (i.e., in the central part of the sample), where the absolute gradient of strain and temperature is assumed to be negligible. Vickers hardness measurements were carried out using a HMV-G20DT microhardness tester (Shimadzu, Kyoto, Japan) with a load of 9.8 N for 15 s. The obtained values correspond to an average at least 5 different indentations measured in the center of the polished sample.

3. Results and Discussion

3.1. Kinetics of Dynamic Transformation

3.1.1. Phase Content during Deformation

Figure 2 presents a compilation of diagrams illustrating the overall microstructural evolution of $DT_{(\gamma \rightarrow \alpha b)}$ as a function of strain. Data displayed in this way allow comprehensive analysis of the phase transformation kinetics during and after the compression. The values displayed at $\epsilon = 0$ refer to microstructure formed after the intermediate holding

step. The grey shaded area denotes the elastic regime of austenite at 500 °C, which was determined using a yield strength of 132 MPa, calculated according to the model proposed by Bohemen [24].

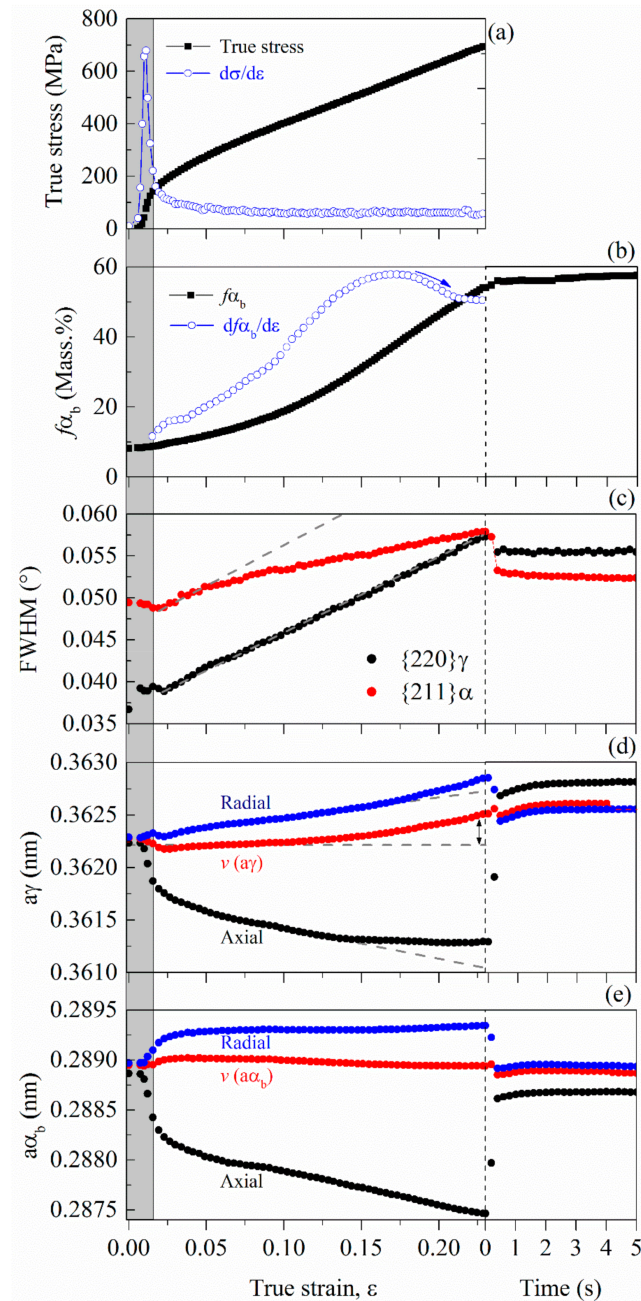


Figure 2. Microstructural evolution of $DT_{(\gamma \rightarrow \alpha_b)}$ at 500 °C as a function of strain and after unloading as a function of time—(a) macroscopic stress; (b) transformed volume fraction of bainitic ferrite- f_{α_b} , (c) full width at half maximum (FWHM) of the $\{220\}\gamma$ and $\{211\}\alpha$ diffraction peaks, (d) austenite lattice parameter- a_γ , and (e) bainitic ferrite lattice parameter- a_{α_b} . “ $\nu(a_\gamma)$ ” and “ $\nu(a_{\alpha_b})$ ” denote the lattice parameter of austenite and bainite considering the Poisson’s ratio, respectively. (Color figure online).

In the elastic regime, after the peak, the continuously decreasing of the strain hardening rate ($d\sigma/d\varepsilon$ curve in Figure 2a) primarily comprises a dynamic recovery regime [25], subsequently reaching a steady state with the imposed strain. The occurrence of the dynamic recovery is seemingly not responsible for the initiation of the DT since the amount of

bainite given in Figure 2b does not evolve significantly in the elastic regime. After the onset of the predicted yielding point, it becomes evident that the plastic deformation triggers the $DT_{(\gamma \rightarrow \alpha_b)}$ (Figure 2b). The volume fraction of the bainite produced by deformation increases continuously from 8% to about 54%. The transformation rate (curve $df_{\alpha_b}/d\varepsilon$) displays a monotonic trend from $\varepsilon \sim 0.015$ up to about $\varepsilon \sim 0.16$, thus evidencing different kinetics over this range. The linear increase of the macroscopic stress up to 690 MPa strongly suggests that austenite was transformed into a phase with higher strength (bainitic ferrite) over the course of deformation. Otherwise, even at a strain rate of 0.05 s^{-1} the deformation of a fully austenitic sample at $500 \text{ }^\circ\text{C}$ would reach $\sim 460 \text{ MPa}$ (see Figure S1 of Supplementary Material). The obtained volume fraction of bainite during the deformation cycle was not reported in the few available studies on the topic [3,4,9]. Therefore, a direct comparison with the present results is not possible. On the other hand, there is a reasonable agreement regarding the dynamic transformation starting right after the yield point has been achieved [4], but at a much lower temperature than $500 \text{ }^\circ\text{C}$. Also, no other investigation reports evidence of $DT_{(\gamma \rightarrow \alpha_b)}$ at or close to $500 \text{ }^\circ\text{C}$.

It is important to point out that the uniaxial compression was carried out in the non-recrystallization region, thus austenite grain size remains unchanged during deformation. Furthermore, α_b subunits (formed during the intermediate holding step) are expected to nucleate at γ grain boundaries [26,27]. During the subsequent compression, the presence of such subunits could inhibit or delay a modification in the austenite grain boundary area via pinning the grain boundaries. Therefore, in the present investigation it will be assumed that possible changes in austenite grain boundaries have a negligible effect during the dynamic transformation.

The growth of bainite during deformation is in contrast to what is generally documented in the literature, which reports that plastic deformation hinders the progress of transformation due to mechanical stabilization of austenite [1,6,28,29]. Besides, the driving force for bainite nucleation close to $500 \text{ }^\circ\text{C}$ under isothermal condition is very low, which would generally result in a relatively small volume fraction (as will be discussed later). In the present study, the growth of bainite under plastic deformation regime can be ascribed to the generation of *dynamic* dislocations, where the term “*dynamic*” is used to describe a scenario of continuous change in mobility and density of dislocations within the austenite during DT. In the mentioned scenario, it is expected that mobile dislocations increase the ability of plastic- and self-accommodation of the α_b/γ interfaces during the growth of bainite laths, besides preventing the local accumulation of the microstructural defects against the bainitic substructures, and thus assisting the dynamic transformation. The argument on the role of dislocations in DT is strengthened by the fact that previous investigations on a bainitic steel suggest that the dislocation substructures introduced in austenite before phase transformation strongly influence bainite kinetics under isothermal conditions [14,30].

It seems reasonable to argue that interactions between α_b subunits and dislocations during deformation reflect the monotonic increase observed in the transformation rate ($df_{\alpha_b}/d\varepsilon$) up to $\varepsilon \sim 0.16$ in Figure 2b. Furthermore, when the bainite fraction exceeds a critical value during DT, the local mobility of dislocations in the remaining austenite becomes more difficult due to the geometrical constraint effect of the bainitic matrix and the work hardening effect on the surrounding austenite, explaining the observable decrease in the transformation rate above $\varepsilon \sim 0.17$. This decrease also suggests the possibility that the transformation is reaching its end. However, it is not clear if the transformation stasis occurs under deformation, since no additional strain could be applied due to the technical limitations of the dilatometer. Immediately after the deformation step, the volume fraction f_{α_b} does not change significantly with time, possibly because no further dislocations are induced in austenite.

3.1.2. Peak Broadening

Figure 2c shows the FWHM evolution of the austenite and bainitic ferrite diffraction peaks during the macroscopic deformation. Firstly, in order to understand the studied phenomena, the diffraction peak broadening during the bainitic reaction was evaluated under an isothermal condition at 430 °C without deformation (in situ HEXRD experiment is reported in the Supplementary Material). The reason for such an experiment is because of the relatively sluggish kinetics of the bainitic reaction in the reference condition (isothermal treatment at 500 °C ($\epsilon = 0$), which will be discussed later). The broadening evolution of the $\{211\}\alpha$ peak is almost constant after the onset of bainite formation at 430 °C ($f_{\alpha_b} \approx 9$ Mass.%), whereas the broadening in the $\{220\}\gamma$ reflection increases significantly after $f_{\alpha_b} > 39$ Mass.% (see Supplementary Material Figure S2). Such increase in the $\{220\}\gamma$ peak reflects the generation of dislocations in the parent austenite induced by the progress of the bainitic transformation itself.

In Figure 2c, the increase in the FWHM during macroscopic strain points out changes in the dislocation structure and density in both bainitic ferrite and austenite during DT. Comparing the rate of broadening between the studied reflections, the higher rate observed in the $\{220\}\gamma$ family grains suggests that the lattice defects are accumulated in the austenite during deformation. Such defects are generated by the superimposed effect of plastic deformation and the bainitic transformation itself. In this scenario, the resulting dislocation debris introduced into the austenite can be inherited by any bainite that forms subsequently [31], which would explain the unexpected constant increase in the FWHM of $\{211\}\alpha$ during the progress of the transformation. Furthermore, as austenite is continuously plastically deformed, the generation of inhomogeneous elastic strains in the already formed α_b subunits might be an additional contribution to the broadening of the $\{211\}\alpha$ reflection during DT.

As already mentioned, the volume fraction of bainite is not expected to have a large influence in the broadening of $\{220\}\gamma$ reflection until a significant progress of the phase transformation occurs under pure isothermal conditions (e.g., $f_{\alpha_b} > 39$ Mass.% at 430 °C—see Supplementary Material Figure S2). If such behavior is assumed during DT, the observed diffraction peak broadening in Figure 2c below $\epsilon \sim 0.17$ ($f_{\alpha_b} < 39$ Mass.%) is mainly associated with the plastic deformation of austenite rather than the bainitic transformation itself. Taking into account that the occurrence of plastic deformation can be resolved by observing diffraction peak broadening [32], the higher rate observed in the austenite suggests that plastic strain concentrates on the austenite and not on the surrounding bainitic ferrite formed during the first stages of DT. Besides, the significant decrease in peak broadening rate in the $\{211\}\alpha$ reflection after $\epsilon \sim 0.05$ is a further indication that lattice defects are accumulated in the austenite.

After $DT_{(\gamma \rightarrow \alpha_b)}$, the FWHM of the peaks recovers, meaning that the dislocation network progressively built in both phases during the DT is not permanent. This result can be explained in the context of the thermally activated recovery mechanisms [33] considering the relative high transformation temperature. The magnitude of decrease observed in the $\{220\}\gamma$ is significantly lower than of bainite, providing further evidence of the strain accumulation in austenite after $DT_{(\gamma \rightarrow \alpha_b)}$.

3.1.3. Lattice Parameter

The evolution of the average lattice parameter of austenite (a_γ) and bainitic ferrite (a_{α_b}) during and after the $DT_{(\gamma \rightarrow \alpha_b)}$ is given in Figure 2d,e, respectively. The lattice of both phases at the axial position decreases continuously after passing the yield strength until $\epsilon \sim 0.15$. As the deformation increases, the austenite lattice parameter starts to deviate from the linearity (straight dashed lines) in all azimuthal directions. By comparing Figure 2d,e, it is possible to conclude that no deviation from linearity occurs during the evolution of a_{α_b} . The main factors that may influence a_γ are—carbon content, stress state, temperature, and carbides formation. As demonstrated in Figure 3a, carbides peaks cannot be distinguished from the background in the diffraction patterns during the deformation cycle, otherwise

carbon atoms would be consumed by the carbides leading to a significant decrease in the lattice parameter of austenite [16,34]. Although no clear evidence of carbides was identified, cluster formation or transition carbides with fractions below 1 Mass.% cannot be excluded.

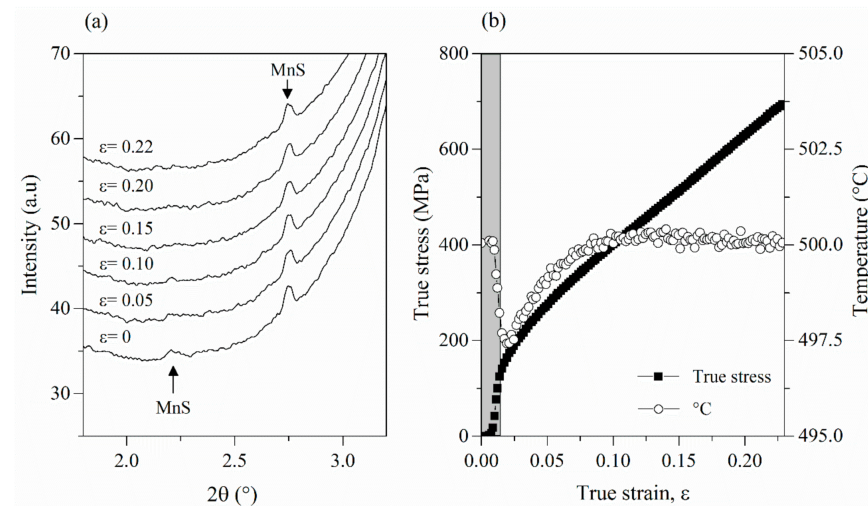


Figure 3. (a) Sequence of the integrated diffraction patterns as a function of strain during the dynamic transformation of bainite at 500 °C. The scale was enlarged in the X-axis in the 2θ range where carbides are expected to appear. The diffraction peaks of manganese sulfide (MnS) are indicated by the arrow. (b) Temperature evolution of the sample during deformation. For reference, the true stress curve is also displayed in this figure. The grey shaded area represents the elastic regime of the austenite at 500 °C.

Figure 3b shows the changes in the temperature measured by the thermocouple during deformation. At the beginning of compression, the maximum temperature variation is about 2.5 °C. This slight fluctuation is probably associated with a small heat loss between the sample/sample holders due to the applied force. This experimental artifact has negligible influence in the microstructural evolution and, therefore, is not responsible for the non-linearity of the $\alpha\gamma$ observed in Figure 2d.

The changes in austenite lattice parameters during DT originate from two contributions—the lattice strain induced by the macroscopic deformation and a change in austenite mean carbon content. Since Figure 2b shows a continuous increase in f_{α_b} during $DT_{(\gamma \rightarrow \alpha_b)}$, carbon partitioning from α_b to γ is expected. Considering that carbon causes a lattice expansion [34], such contribution may act as an opposite effect to the lattice strain imposed by macroscopic deformation, implying that the observed non-linearity of $\alpha\gamma$ is due to carbon enrichment of austenite. The latter has an isotropic effect in the γ lattice parameter (e.g., carbon expands equally the lattice in the axial and radial directions), whereas the lattice strain induced by the macroscopic deformation is essentially anisotropic. Both contributions can be separated using the approach given in [35], which is based on the relation between axial to radial lattice parameters considering Poisson's ratio (ν). For the present case at 500 °C, the ratio of axial to radial slopes gives a Poisson's ratio of 0.281 for austenite. For bainitic ferrite, a value of 0.274 at 500 °C was adopted from [36].

As illustrated in Figure 2d, a significant increase of $\nu(\alpha\gamma)$ from $\epsilon \sim 0.13$ ($f_{\alpha_b} \sim 25$ Mass.%) corroborates the carbon partitioning from α_b to γ during DT, and thus explains the deviation from linearity of $\alpha\gamma$. It is important to note that $\nu(\alpha\gamma)$ is indirect evidence of the increase in the mean carbon concentration in austenite, not accounting for the local variations in composition, which explains why $\nu(\alpha\gamma)$ does not vary significantly during the initial stages of DT. In Figure 2d, during the subsequent unloading, the axial and radial ν reach stable values, substantially higher than those at the beginning of DT. It should be noted that the value of $\nu(\alpha\gamma)$ does not decrease during the unloading, indicating that the remaining austenite was carbon-enriched during deformation.

In contrast to the $\alpha\gamma$ behavior, the observed trends in the axial and radial $\alpha\alpha_b$ in Figure 2e are probably a consequence of the constraint effect from surrounding austenite during the compressive deformation, since the value of $v(\alpha\alpha_b)$ does not increase or decrease significantly during and after $DT_{(\gamma \rightarrow \alpha b)}$. Such behavior suggests indirect evidence that no significant change in partitioning behavior of alloying elements occurs during $DT_{(\gamma \rightarrow \alpha b)}$. Otherwise, a noticeable change from para (only carbon partitioning) to ortho-equilibrium (partitioning of all alloying elements) would be followed by a permanent decrease in the $\alpha\alpha_b$ (axial) after deformation, due to the diffusion of substitutional elements from $\alpha_b \rightarrow \gamma$. This explanation is analogous to that reported by Shibata et al. [37] in the dynamic ferrite transformation, in which deformation accelerates the manganese diffusion from ferrite to austenite, leading to a permanent decrease in lattice constant of DT-ferrite after compression. As already mentioned, the experimental results in Figure 2e suggest that the constraint effect from surrounding austenite is the main mechanism that affects the $\alpha\alpha_b$ lattice parameter during DT.

3.2. Lattice Strains during Dynamic Transformation

The microstructure response during the $DT_{(\gamma \rightarrow \alpha b)}$ and the subsequent unloading from the viewpoint of the lattice strains is summarized in Figure 4. This data provide additional evidence for the lattice parameter results of both phases, previously discussed. The non-linearity in the $\{220\}\gamma$ lattice strain is perceived in both axial and radial directions during the $DT_{(\gamma \rightarrow \alpha b)}$. The peak shift produced by alloy element partitioning was separated from the mechanical strain using the same approach described earlier for the lattice parameter. In Figure 4a,b, the evolution of $v(\epsilon_\gamma)$ is congruent with the tendency shown by the lattice parameter— $v(\alpha\gamma)$ in Figure 2d during and after the deformation. This further evidence from the individual $\{hkl\}$ supports that the non-linearity in the austenite lattice is attributed to the increase in carbon content in solution in austenite during the $DT_{(\gamma \rightarrow \alpha b)}$. From Figure 4c, the value of $v(\epsilon_{\alpha b})$ does not evolve substantially during the compression. Upon unloading, lattice strains of the $\{211\}\alpha$ family grains are almost entirely reversible in the axial and parallel directions, while $v(\epsilon_{\alpha b})$ remains constant (Figure 4d). These observations confirm the already described behavior from the lattice parameter— $v(\alpha\alpha_b)$, suggesting no significant change in partitioning behavior of alloying elements during $DT_{(\gamma \rightarrow \alpha b)}$.

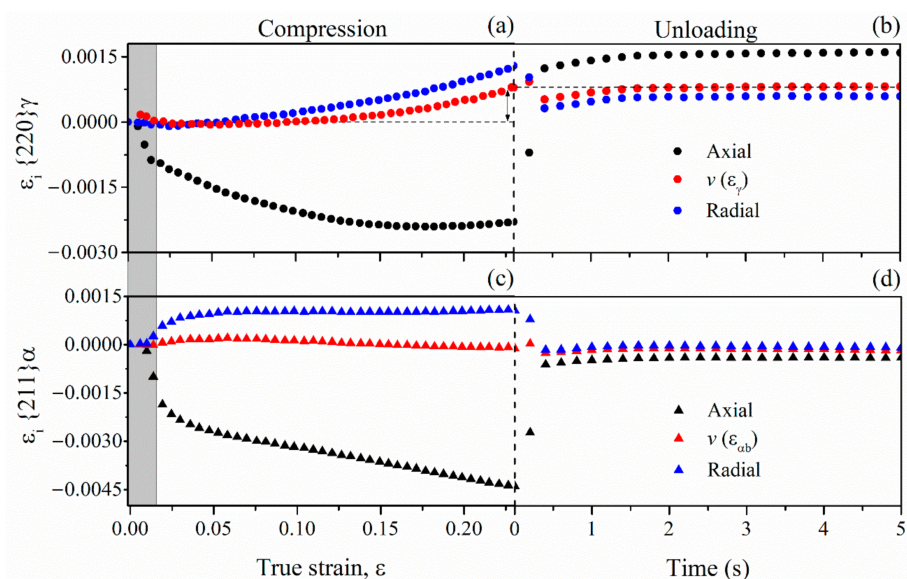


Figure 4. Lattice strains during DT in austenite (a,b) and bainitic ferrite (c,d) as a function of strain and after unloading as a function of time at 500 °C. “ $v(\epsilon_\gamma)$ ” and “ $v(\epsilon_{\alpha b})$ ” denote the lattice strains of austenite and bainite considering the Poisson’s ratio, respectively. (Color figure online).

3.3. Kinetics of Phase Transformation during DT and Isothermal Transformation

Figure 5 shows the volume fraction of bainitic ferrite (f_{α_b}) as a function of time during DT ($\gamma \rightarrow \alpha_b$) in comparison with a reference sample (without deformation). The results show that the austenite decomposition is accelerated (about 11 times faster) during the deformation when compared with the reference condition (without deformation at 500 °C). Additional evidence of the faster bainite formation kinetics during the DT is presented in Figure 6, which compares the microstructural evolution without and with deformation at 500 °C (left and right diagrams, respectively). It can be observed that no significant variation occurs in both FWHM of the peaks (Figure 6a) and lattice parameters (Figure 6b,c) in the undeformed condition. Therefore, it can be concluded that the observed tendencies during deformation in Figure 6d–f are direct consequences of the mechanisms that rule the dynamic transformation of austenite to bainite.

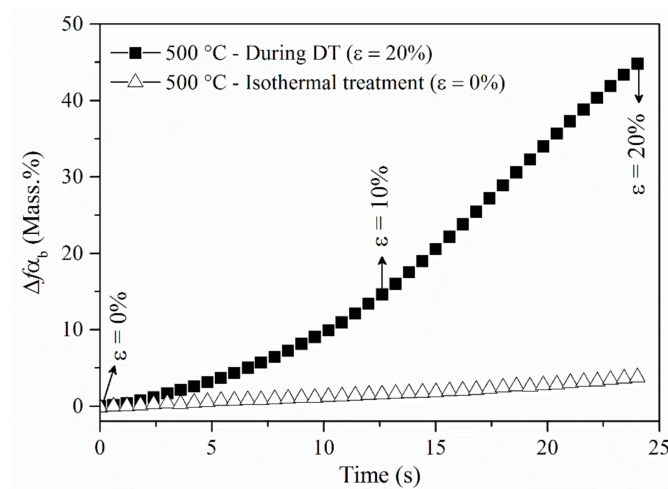


Figure 5. Changes in volume fraction of bainitic ferrite during DT ($\gamma \rightarrow \alpha_b$) at 500 °C (squares) in contrast with a reference sample without deformation at 500 °C (triangles). Note that volume fractions are displayed as “ Δ ” from the starting point $t = 0$ s, which is counted after the intermediate holding step (see the inset of Figure 1a). Deformation stages (0, 10 and 20%) for DT are indicated in this figure.

The relatively slow bainite formation kinetics during the treatment without the deformation is explained by the low driving force for nucleation close to 500 °C, since the isothermal bainite formation kinetics mainly depend on the rate of bainite nucleation [27,38]. Therefore, increasing nucleation sites for bainite formation due to deformation is expected to be the main reason for the acceleration effect from DT. As previously discussed in Figure 2c, the applied strain concentrates on austenite during plastic deformation. Thus, it is expected that numerous microstructural defects, such as dislocations, are progressively introduced into austenite as the strain increases. In this scenario, the kinetics of the bainitic transformation is accelerated by increasing the initial number density of potential nucleation sites for bainite [6,14], besides increasing the local carbon diffusivity in austenite [39]. Increased nucleation rate is also suggested as the main mechanism which boosts dynamic transformations (e.g., [37,39–42]). According to the literature, when the stress exceeds the yield strength of austenite, the defects introduced by deformation enhance the nucleation rate, and hence the overall rate of bainite reaction increases [43]. It is obvious that the experimental results in Figure 2 confirm the statement above—plastic deformation induces defects in austenite (affecting austenite peak broadening in Figure 2c), which in turn triggers the bainite formation (Figure 2b). Therefore, it is suggested that the acceleration effect of DT is due to increased nucleation rate in austenite, rather than solely the accelerated growth of the previous nuclei formed during the intermediate holding step.

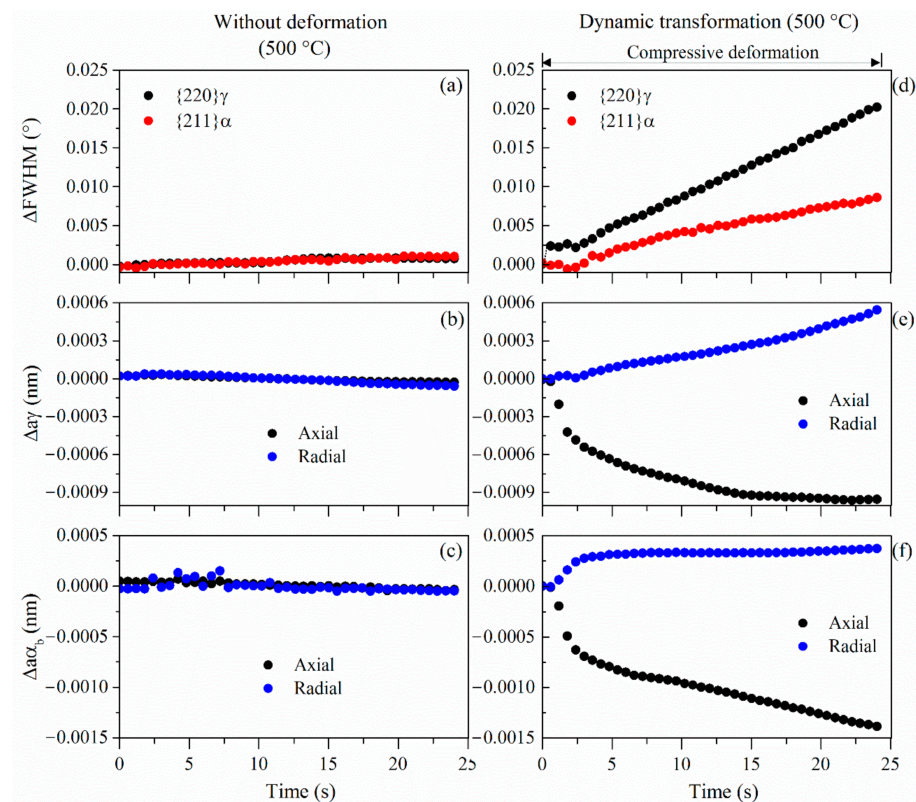


Figure 6. Evolution of the microstructural parameters at 500 °C during bainitic transformation without compression (left diagrams) and during dynamic transformation (right diagrams)—(a,d) FWHM of the $\{220\}\gamma$ and $\{211\}\alpha$ diffraction peaks; (b,e) austenite lattice parameter; (c,f) bainitic ferrite lattice parameter. Note that all datasets are displayed as “ Δ ” from the starting point $t = 0$ s, which is counted after the intermediate holding step (see the inset of Figure 1a).

Based on the real-time evidence, it is proposed that the $DT_{(\gamma \rightarrow \alpha b)}$ is governed by the preferential introduction of dynamic dislocations in austenite (e.g., dislocations simultaneously provide additional nucleation sites for bainite as well as assist the progress of the dynamic transformation).

3.4. Ex-Situ Microstructure

Figure 7 shows representative SEM micrographs of the investigated samples in the undeformed condition (Figure 7a—isothermally formed at 500 °C followed by continuous cooling to room temperature) and deformed (Figure 7b—dynamic transformation at 500 °C followed by continuous cooling to room temperature). The obtained microstructures are granular bainite with a considerable amount of retained austenite (undeformed and deformed samples with 15.5 and 12 Mass.%, respectively). Since bainitic ferrite is more attacked by the etchant, the network of structures that appear to be elevated in the micrographs are attributed to the retained austenite or martensite–austenite (M/A) constituents [1,15,44]. The hardness of the undeformed sample is 368 ± 12 (HV1), while that of deformed one (dynamically formed) reaches 420 ± 10 (HV1). Considering that both micrographs contain only bainitic microstructures, the hardness increase in the deformed sample can be associated with its finer microstructure (Figure 7b) due to the increased number of nucleation sites promoted by plastic deformation. Besides, considering that austenite is simultaneously strengthened and decomposed into bainite, it is expected that a structural refinement takes place in the bainite coming from dynamic transformation. This argument is supported by the fact that strength of the parent austenite is one of the most important factors that control the scale of the bainitic microstructures [45,46]. The hardness results seem to be in contradiction with the ones from [4], which reports that the presence

of phases formed during the compression step reduces the hardness value of the bainitic microstructures in comparison with the pure isothermal condition.

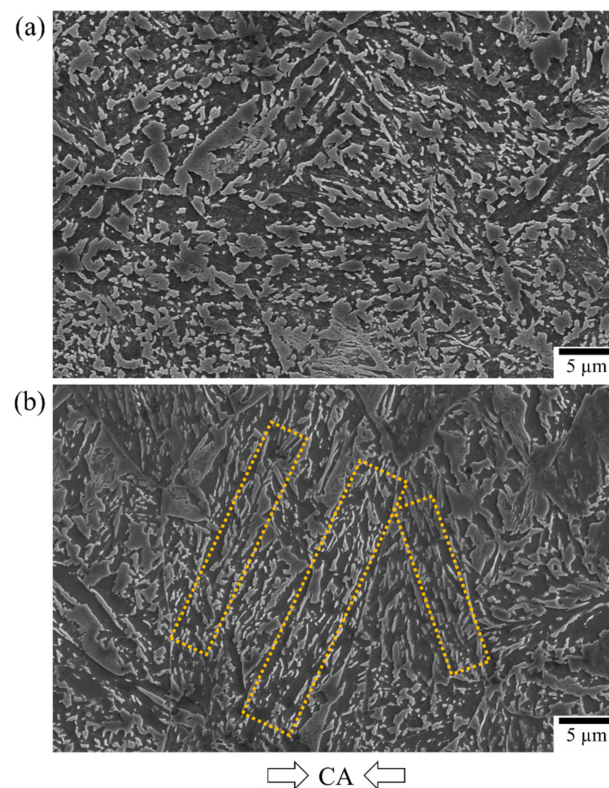


Figure 7. SEM micrographs of the processed samples—(a) undeformed condition (isothermally formed at 500 °C followed by continuous cooling to room temperature). (b) Deformed condition (dynamic transformation at 500 °C followed by continuous cooling to room temperature). CA stands for the compression axis.

In Figure 7, although both microstructures share similar features of the granular bainite (e.g., discontinuous network of retained austenite and M/A constituents), it is possible to conclude that the microstructure in the reference sample (undeformed condition at 500 °C—Figure 7a) appears to be more randomly oriented. In contrast, the network of structures in the deformed sample seems to be more preferentially oriented perpendicularly to the loading direction (as indicated by dashed rectangles). Considering that a significant amount of bainitic ferrite (46 Mass.%) was induced by strain, combined with the fact that plastic deformation during phase transformation alters the average scale of the microstructure [4,8], it seems plausible to suggest that the microstructure develops perpendicular to the compression during $DT_{(\gamma \rightarrow \alpha b)}$.

4. Conclusions

In summary, this work reveals for the first time the microstructural evolution of DT of austenite to bainite employing in situ HEXRD measurements during uniaxial compression at 500 °C. The main conclusions, for the studied conditions in the investigated steel, are:

- The kinetics of bainite is accelerated through $DT_{(\gamma \rightarrow \alpha b)}$ at 500 °C in comparison with pure isothermal treatment;
- Plastic deformation triggers the $DT_{(\gamma \rightarrow \alpha b)}$, which is continuously stimulated because lattice defects are introduced preferentially in the austenite;
- Based on real-time evidence, it was proposed that the $DT_{(\gamma \rightarrow \alpha b)}$ is ruled by the dynamic introduction of dislocations, which enable the progress of the transformation without mechanical stabilization of austenite;

- The partitioning of alloying elements during DT is suggested to occur under paraequilibrium conditions (i.e., only carbon partitioning);
- The bainitic microstructure in the sample subjected to $DT_{(\gamma \rightarrow \alpha b)}$ is preferentially oriented perpendicular to the compression direction. Furthermore, both microstructural refinement and hardness increase were obtained in comparison with the reference microstructure; and
- It is important to emphasize that even though the strain rate employed in the present investigation does not necessarily reflect typical values applied in the industrial warm forgings and/or controlled rolling processes, the $DT_{(\gamma \rightarrow \alpha b)}$ may represent a potential strategy aiming at energy-efficient manufacturing processes, since phase transformation and plastic deformation are taking place simultaneously. Besides, $DT_{(\gamma \rightarrow \alpha b)}$ sheds new insights into design carbide-free bainitic microstructures via thermomechanical processing.

Supplementary Materials: The following are available online at <https://www.mdpi.com/2075-4701/11/3/467/s1>, Figure S1: True stress-strain curves of the samples deformed in compression up to 20% at 500 °C: strain rate of 0.01 s^{-1} (partially austenitic microstructure) and 0.05 s^{-1} (fully austenitic microstructure), Figure S2: (a) Bainitic ferrite volume fraction as a function of time during isothermal holding at 430 °C (without deformation). For reference, the FWHM of the austenite and bainitic ferrite diffraction peaks is also displayed in this plot. (b) Detailed view of (a) showing the onset of the transformation. The reference time ($t = 0 \text{ s}$) corresponds to the moment at which a temperature of 430 °C is reached during cooling.

Author Contributions: Conceptualization, J.D., J.E. and W.L.B.; Methodology, J.D., W.L.B., H.M. and J.E.; Validation, W.L.B.; Formal Analysis, W.L.B., H.M. and J.E.; Investigation, J.D., J.E., W.L.B. and H.M.; Writing—Original Draft Preparation, W.L.B.; Writing—Review and Editing, J.E., H.R., H.M., J.D., A.d.S.R. and A.R.; Visualization, W.L.B.; Project Administration, J.D., J.E. and A.d.S.R.; Funding Acquisition, J.E. and A.d.S.R. All authors have read and agreed to the published version of the manuscript.

Funding: This research was financed in part by the Coordenação de Aperfeiçoamento de Pessoal de Nível Superior—Brasil (CAPES)—Finance Code 001 and the Deutsche Forschungsgemeinschaft_DFG (EP 128/6-2) via Project number 327887503.

Institutional Review Board Statement: Not applicable.

Informed Consent Statement: Not applicable.

Data Availability Statement: Not applicable.

Acknowledgments: The authors gratefully acknowledge DESY for the provision of beamtime and Norbert Schell and Andreas Stark from Helmholtz-Center-Geesthacht at beamline P07 (PETRA III-DESY) for support during the synchrotron experiments. W.L.B. thanks to Coordenação de Aperfeiçoamento de Pessoal de Nível Superior (CAPES—Grant number 1844/2017/process 88881.142485/2017-01) for the scholarship.

Conflicts of Interest: The authors declare no conflict of interest.

References

1. Lemos Bevilaqua, W.; Epp, J.; Meyer, H.; Da Silva Rocha, A.; Roelofs, H. In Situ Investigation of the Bainitic Transformation from Deformed Austenite During Continuous Cooling in a Low Carbon Mn-Si-Cr-Mo Steel. *Metall. Mater. Trans. A* **2020**, *51*, 3627–3637. [[CrossRef](#)]
2. Silveira, A.C.d.F.; Bevilaqua, W.L.; Dias, V.W.; de Castro, P.J.; Epp, J.; Rocha, A.d.S. Influence of Hot Forging Parameters on a Low Carbon Continuous Cooling Bainitic Steel Microstructure. *Metals* **2020**, *10*, 601. [[CrossRef](#)]
3. Kaikkonen, P.M.; Somani, M.C.; Miettunen, I.H.; Porter, D.A.; Pallaspuuro, S.T.; Kömi, J.I. Constitutive flow behaviour of austenite at low temperatures and its influence on bainite transformation characteristics of ausformed medium-carbon steel. *Mater. Sci. Eng. A* **2020**, *775*, 12. [[CrossRef](#)]
4. Eres-Castellanos, A.; Caballero, F.G.; Garcia-Mateo, C. Stress or strain induced martensitic and bainitic transformations during ausforming processes. *Acta Mater.* **2020**, *189*, 60–72. [[CrossRef](#)]

5. He, J.; Du, J.; Zhang, W.; Zhang, C.; Yang, Z.-G.; Chen, H. Abnormal Anisotropic Dilatation During Bainitic Transformation of Ausformed Austenite. *Metall. Mater. Trans. A* **2019**, *50*, 540–546. [[CrossRef](#)]
6. van Bohemen, S.M.C. Bainite growth retardation due to mechanical stabilisation of austenite. *Materialias* **2019**, *7*, 17. [[CrossRef](#)]
7. Zhao, L.; Qian, L.; Zhou, Q.; Li, D.; Wang, T.; Jia, Z.; Zhang, F.; Meng, J. The combining effects of ausforming and below- M_s or above- M_s austempering on the transformation kinetics, microstructure and mechanical properties of low-carbon bainitic steel. *Mater. Des.* **2019**, *183*, 108–123. [[CrossRef](#)]
8. Eres-Castellanos, A.; Hidalgo, J.; Zorgani, M.; Jahazi, M.; Toda-Caraballo, I.; Caballero, F.G.; Garcia-Mateo, C. Assessing the scale contributing factors of three carbide-free bainitic steels: A complementary theoretical and experimental approach. *Mater. Des.* **2021**, *197*, 15. [[CrossRef](#)]
9. Eres-Castellanos, A.; Morales-Rivas, L.; Latz, A.; Caballero, F.G.; Garcia-Mateo, C. Effect of ausforming on the anisotropy of low temperature bainitic transformation. *Mater. Charact.* **2018**, *145*, 371–380. [[CrossRef](#)]
10. Guo, L.; Bhadeshia, H.K.D.H.; Roelofs, H.; Lembke, M.I. In situ synchrotron X-ray study of bainite transformation kinetics in a low-carbon Si-containing steel. *Mater. Sci. Technol.* **2017**, *33*, 2147–2156. [[CrossRef](#)]
11. Onuki, Y.; Hirano, T.; Hoshikawa, A.; Sato, S.; Tomida, T. In Situ Observation of Bainite Transformation and Simultaneous Carbon Enrichment in Austenite in Low-Alloyed TRIP Steel Using Time-of-Flight Neutron Diffraction Techniques. *Metall. Mater. Trans. A* **2019**, *50*, 4977–4986. [[CrossRef](#)]
12. Rementeria, R.; Jimenez, J.A.; Allain, S.Y.P.; Geandier, G.; Poplawsky, J.D.; Guo, W.; Urones-Garrote, E.; Garcia-Mateo, C.; Caballero, F.G. Quantitative assessment of carbon allocation anomalies in low temperature bainite. *Acta Mater.* **2017**, *133*, 333–345. [[CrossRef](#)]
13. Babu, S.S.; Specht, E.D.; David, S.A.; Karapetrova, E.; Zschack, P.; Peet, M.; Bhadeshia, H.K.D.H. In-situ observations of lattice parameter fluctuations in austenite and transformation to bainite. *Metall. Mater. Trans. A* **2005**, *36*, 3281–3289. [[CrossRef](#)]
14. Gong, W.; Tomota, Y.; Adachi, Y.; Paradowska, A.M.; Kelleher, J.F.; Zhang, S.Y. Effects of ausforming temperature on bainite transformation, microstructure and variant selection in nanobainite steel. *Acta Mater.* **2013**, *61*, 4142–4154. [[CrossRef](#)]
15. Reisinger, S.; Kozeschnik, E.; Ressel, G.; Keckes, J.; Stark, A.; Marsoner, S.; Ebner, R. Strain energy contributions on the bainitic phase transformation in a CrMoV steel during continuous cooling. *Mater. Des.* **2018**, *155*, 475–484. [[CrossRef](#)]
16. Shi, Z.; Tomota, Y.; Harjo, S.; Su, Y.; Chi, B.; Pu, J.; Jian, L. Effect of non-isothermal deformation of austenite on ferrite transformation behavior studied by in-situ neutron diffraction. *Mater. Sci. Eng. A* **2015**, *631*, 153–159. [[CrossRef](#)]
17. Dutta, R.K.; Huizenga, R.M.; Amirthalingam, M.; Gao, H.; King, A.; Hermans, M.J.M.; Richardson, I.M. In-situ synchrotron diffraction studies on hot deformation of austenite in a high strength quenched and tempered structural steel. *Adv. Mater. Res.* **2014**, *922*, 126–131. [[CrossRef](#)]
18. Epp, J.; Dong, J.; Meyer, H.; Bohlen, A. Analysis of cyclic phase transformations during additive manufacturing of hardenable tool steel by in-situ X-ray diffraction experiments. *Scr. Mater.* **2020**, *177*, 27–31. [[CrossRef](#)]
19. Barriobero-Vila, P.; Gussone, J.; Kelm, K.; Haubrich, J.; Stark, A.; Schell, N.; Requena, G. An in situ investigation of the deformation mechanisms in a β -quenched Ti-5Al-5V-5Mo-3Cr alloy. *Mater. Sci. Eng. A* **2018**, *717*, 134–143. [[CrossRef](#)]
20. van Bohemen, S.M.C.C. Bainite and martensite start temperature calculated with exponential carbon dependence. *Mater. Sci. Technol.* **2011**, *28*, 487–495. [[CrossRef](#)]
21. Ashiotis, G.; Deschildre, A.; Nawaz, Z.; Wright, J.P.; Karkoulis, D.; Picca, F.E.; Kieffer, J. The fast azimuthal integration Python library: PyFAI. *J. Appl. Crystallogr.* **2015**, *48*, 510–519. [[CrossRef](#)]
22. He, S.H.; He, B.B.; Zhu, K.Y.; Huang, M.X. Evolution of dislocation density in bainitic steel: Modeling and experiments. *Acta Mater.* **2018**, *149*, 46–56. [[CrossRef](#)]
23. Allain, S.Y.P.; Gaudez, S.; Geandier, G.; Danoix, F.; Soler, M.; Goune, M. Carbon heterogeneities in austenite during Quenching & Partitioning (Q&P) process revealed by in situ High Energy X-ray Diffraction (HEXRD) experiments. *Scr. Mater.* **2020**, *181*, 108–114. [[CrossRef](#)]
24. van Bohemen, S.M.C. Exploring the correlation between the austenite yield strength and the bainite lath thickness. *Mater. Sci. Eng. A* **2018**, *731*, 119–123. [[CrossRef](#)]
25. Kalidindi, S.R. Modeling the strain hardening response of low SFE FCC alloys. *Int. J. Plast.* **1998**, *14*, 1265–1277. [[CrossRef](#)]
26. Ravi, A.M.; Navarro-López, A.; Sietsma, J.; Santofimia, M.J. Influence of martensite/austenite interfaces on bainite formation in low-alloy steels below M_s . *Acta Mater.* **2020**, *188*, 394–405. [[CrossRef](#)]
27. Ravi, A.M.; Sietsma, J.; Santofimia, M.J. Exploring bainite formation kinetics distinguishing grain-boundary and autocatalytic nucleation in high and low-Si steels. *Acta Mater.* **2016**, *105*, 155–164. [[CrossRef](#)]
28. Hu, H.; Zurob, H.S.; Xu, G.; Embury, D.; Purdy, G.R. New insights to the effects of ausforming on the bainitic transformation. *Mater. Sci. Eng. A* **2015**, *626*, 34–40. [[CrossRef](#)]
29. Larn, R.H.; Yang, J.R. The effect of compressive deformation of austenite on the bainitic ferrite transformation in Fe-Mn-Si-C steels. *Mater. Sci. Eng. A* **2000**, *278*, 278–291. [[CrossRef](#)]
30. Gong, W.; Tomota, Y.; Koo, M.S.; Adachi, Y. Effect of ausforming on nanobainite steel. *Scr. Mater.* **2010**, *63*, 819–822. [[CrossRef](#)]
31. Bhadeshia, H.K.D.H.; Christian, J.W. Bainite in steels. *Metall. Trans. A* **1990**, *21*, 767–797. [[CrossRef](#)]
32. Hidalgo, J.; Huizenga, R.M.; Findley, K.O.; Santofimia, M.J. Interplay between metastable phases controls strength and ductility in steels. *Mater. Sci. Eng. A* **2019**, *745*, 185–194. [[CrossRef](#)]

33. Brandstetter, S.; Budrović, Ž.; Van Petegem, S.; Schmitt, B.; Stergar, E.; Derlet, P.M.; Van Swygenhoven, H. Temperature-dependent residual broadening of x-ray diffraction spectra in nanocrystalline plasticity. *Appl. Phys. Lett.* **2005**, *87*, 2. [[CrossRef](#)]
34. Ebner, S.; Schnitzer, R.; Suppan, C.; Stark, A.; Liu, H.; Hofer, C. Characterization of carbides in Q&P steels using a combination of high-resolution methods. *Mater. Charact.* **2020**, *163*, 110242. [[CrossRef](#)]
35. Blondé, R.; Jimenez-Melero, E.; Zhao, L.; Wright, J.P.; Brück, E.; van der Zwaag, S.; van Dijk, N.H. High-energy X-ray diffraction study on the temperature-dependent mechanical stability of retained austenite in low-alloyed TRIP steels. *Acta Mater.* **2012**, *60*, 565–577. [[CrossRef](#)]
36. Dutta, R.K.; Huizenga, R.M.; Amirthalingam, M.; King, A.; Gao, H.; Hermans, M.J.M.; Richardson, I.M. In situ synchrotron diffraction studies on the temperature-dependent plane-specific elastic constants in a high-strength quenched and tempered structural steel. *Scr. Mater.* **2013**, *69*, 187–190. [[CrossRef](#)]
37. Shibata, A.; Takeda, Y.; Park, N.; Zhao, L.; Harjo, S.; Kawasaki, T.; Gong, W.; Tsuji, N. Nature of dynamic ferrite transformation revealed by in-situ neutron diffraction analysis during thermomechanical processing. *Scr. Mater.* **2019**, *165*, 44–49. [[CrossRef](#)]
38. Ravi, A.M.; Kumar, A.; Herbig, M.; Sietsma, J.; Santofimia, M.J. Impact of austenite grain boundaries and ferrite nucleation on bainite formation in steels. *Acta Mater.* **2020**, *188*, 424–434. [[CrossRef](#)]
39. Ghosh, C.; Aranas, C.; Jonas, J.J. Dynamic transformation of deformed austenite at temperatures above the Ae3. *Prog. Mater. Sci.* **2016**, *82*, 151–233. [[CrossRef](#)]
40. Park, N.; Zhao, L.; Shibata, A.; Tsuji, N. Dynamic Ferrite Transformation Behaviors in 6Ni-0.1C Steel. *JOM* **2014**, *66*, 765–773. [[CrossRef](#)]
41. Adachi, Y.; Xu, P.G.; Tomota, Y. Crystallography and Kinetics of Dynamic Transformation in Steels. *ISIJ Int.* **2008**, *48*, 1056–1062. [[CrossRef](#)]
42. Guo, B.; Liu, Y.; Jonas, J.J. Dynamic Transformation of Two-Phase Titanium Alloys in Stable and Unstable States. *Metall. Mater. Trans. A* **2019**, *50*, 4502–4505. [[CrossRef](#)]
43. Hase, K.; Garcia-Mateo, C.; Bhadeshia, H.K.D.H. Bainite formation influenced by large stress. *Mater. Sci. Technol.* **2004**, *20*, 1499–1505. [[CrossRef](#)]
44. Reisinger, S.; Ressel, G.; Eck, S.; Marsoner, S. Differentiation of grain orientation with corrosive and colour etching on a granular bainitic steel. *Micron* **2017**, *99*, 67–73. [[CrossRef](#)]
45. Cornide, J.; Garcia-Mateo, C.; Capdevila, C.; Caballero, F.G. An assessment of the contributing factors to the nanoscale structural refinement of advanced bainitic steels. *J. Alloys Compd.* **2013**, *577*, S43–S47. [[CrossRef](#)]
46. Singh, S.B.; Bhadeshia, H.K.D.H. Estimation of bainite plate-thickness in low-alloy steels. *Mater. Sci. Eng. A* **1998**, *245*, 72–79. [[CrossRef](#)]